5

Characterization of Brillouin Gratings in Optical Fibers and Their Applications

Yongkang Dong, Hongying Zhang,
Dapeng Zhou, Xiaoyi Bao and Liang Chen
University of Ottawa
Canada

1. Introduction

There is an increasing interest over recent years in Brillouin gratings in optical fibers due to their applications in optical storage (Cao et al., 2008; Kalosha et al., 2008; Zhu et al., 2007), distributed sensing (Dong et al., 2009; Song et al., 2009, 2010; Zou et al., 2009a, 2009b, 2010), optical delay line (Song et al., 2009), and birefringence characterization of polarization-maintaining fibers (Dong et al., 2010). Generally, a Brillouin grating is generated by using two counter-propagating pump waves through stimulated Brillouin scattering (Song et al., 2008). A Brillouin grating is formed by a moving periodically modulated refractive index associated with an acoustic wave, which is created by two pump waves through electrostriction effect. Compared with conventional fiber Bragg gratings, the Brillouin gratings have two unique features: one is that it is a moving grating, which can produce a Brillouin frequency shift on the reflected light with respect to the probe wave, and the other is that it has a lifetime (~10 ns in a silica fiber) for its existence after removing the two pump waves.

For most applications, a high-birefringence polarization-maintaining fiber is used, where two pump waves are launched into one axis of the polarization-maintaining fiber to create a Brillouin grating and a probe wave is launched into the other axis to read the grating; when the frequency difference between the probe and the pump waves satisfies the phase matching condition, a maximum reflection on the Brillouin grating can be observed. So the process involves four light waves, i. e., two pump waves, a probe wave and a reflected wave, and in fact it is a Brillouin enhanced four-wave mixing process. The interaction between the probe wave and the Brillouin grating involves two cases: one case is that the probe wave propagates in the same direction as the Brillouin grating, so coherent Stokes Brillouin scattering could occur and the reflected wave frequency is lower than that of the probe wave by a Ω_B; the other case is for the counter-propagating between the probe wave and the Brillouin grating, so coherent anti-Stokes Brillouin scattering could occur and the reflected wave is frequency up-converted by a Ω_B with respective to the probe wave. The phase matching condition of the coherent Stokes Brillouin scattering or coherent anti-Stokes Brillouin scattering in a polarization-maintaining fiber is $\Delta\nu_{Bire} = \Delta n\nu / n_g$, where Δn is the phase birefringence of the polarization-maintaining fiber, n_g is the group refractive index, and ν is the frequency of probe wave. $\Delta\nu_{Bire}$ is the birefringence-induced frequency shift

between the probe and pump waves and is proportional to the local birefringence of the polarization-maintaining fiber.

A Brillouin grating can be generated in frequency correlation domain (Zou et al., 2009a, 2009b, 2010) and time domain (Dong et al., 2009, 2010a, 2010b; Song et al., 2008, 2009a, 2009b, 2010), respectively. With the correlation-based technique, a Brillouin grating is generated using two synchronized and frequency-modulated continuous-wave (CW) pump waves. In time domain, a Brillouin grating can be more conveniently generated through two frequency-locked pump waves, which includes three schemes in terms of pump type. The first scheme uses two CW pumps, and the Brillouin grating can exist in the whole fiber for a uniform Brillouin frequency shift over the fiber (Song et al., 2008; Zou et al., 2009), where the length of Brillouin grating would be limited by the coherent length of the pump lasers. The second scheme includes a CW pump and a pump pulse, where the Brillouin grating is generated following the pump pulse from one end to the other end (Song et al., 2009, 2010). In this case, due to the decay of the acoustic wave, the length of the existing Brillouin grating is limited to $L_B = (t_P + \tau_B)c/n$, where t_P is the width of pump pulse, τ_B is the phonon lifetime. The third scheme includes two short pump pulses (< 10 ns), where the Brillouin grating can be generated at a specific location controlled by the delay between the two pump pulses (Dong et al., 2009, 2010). The interaction length of the two pulses is $L = (t_{P1} + t_{P2})c/2n$, where t_{P1} and t_{P2} are the pulse widths of pump 1 and pump 2, respectively. However, due to different phonon excitation time, the effective length of Brillouin grating is only half of the interaction length, i. e. $L_B = (t_{P1} + t_{P2})c/4n$, for example, 20 cm for two 2 ns pump pulses.

This chapter is structured as follows: in the second section, we will give the coupled wave equations of Brillouin enhanced four-wave mixing associated with a Brillouin grating, from which the analytic solution of the steady uniform Brillouin grating spectrum is deduced without pump depletion; in the third section, we will numerically study the Brillouin grating spectrum with a strong probe wave for both coherent Stokes Brillouin scattering and coherent anti-Stokes Brillouin scattering cases; in the fourth section, we will experimentally study the transient Brillouin grating spectrum by using two pump pulses and a probe pulse; in the fifth section, we will introduce two applications of Brillouin gratings, i. e., distributed birefringence measurement of polarization-maintaining fibers and distributed simultaneous temperature and strain measurement; at the end, a conclusion will be given in the sixth section.

2. Coupled wave equations of Brillouin gratings

In this section, the coupled wave equations of Brillouin enhanced four-wave mixing associated with a Brillouin grating are given first. Then the analytic solution of the steady uniform Brillouin grating spectrum is deduced for the case of a weak probe. And last, the phase matching condition for the case of a polarization-maintaining fiber as well as the birefringence-induced frequency shift is discussed.

2.1 Coupled wave equations

The scheme of interaction between the four optical waves and the acoustic wave within a polarization-maintaining fiber is shown in Fig. 1, where the fiber length is along the z

direction, while its two axes are along x and y directions, respectively. In this analysis an acoustic wave of amplitude ρ, frequency Ω, and wave vector **q** is generated by two pump waves, pump1 and pump2, of amplitudes A_1 and A_2, frequencies ω_1 and ω_2, and wave vectors $\mathbf{k}_1$ and $\mathbf{k}_2$ respectively that counter propagate in the x axis of the polarization-maintaining fiber, and ω_1 is larger than ω_2 by a Brillouin frequency shift. Here we discuss the coherent anti-Stokes Brillouin scattering case in which the probe wave of amplitude A_3, frequency ω_3, and wave vector $\mathbf{k}_3$ counter propagates with and scatters off the acoustic wave to form a scattered wave of amplitude A_4, frequency ω_4, and wave vector $\mathbf{k}_4$ in the y axis of the polarization-maintaining fiber.

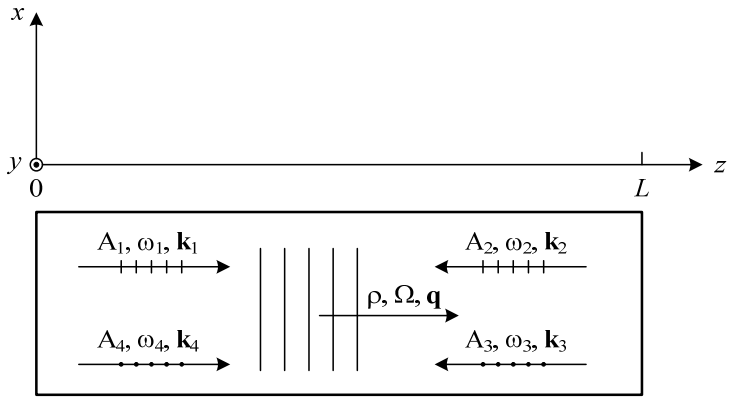

Fig. 1. Scheme of interaction between the optical and acoustic waves in a Brillouin enhanced four-wave mixing process associated with a Brillouin grating.

For the interacting system shown in Fig. 1, the total optical field can be represented as

$$\tilde{E}(z,t) = \tilde{E}_1(z,t) + \tilde{E}_2(z,t) + \tilde{E}_3(z,t) + \tilde{E}_4(z,t) \tag{1}$$

where $\tilde{E}_1(z,t)$, $\tilde{E}_2(z,t)$, $\tilde{E}_3(z,t)$, $\tilde{E}_4(z,t)$ represent pump 1, pump 2, probe and reflection waves, respectively, and can be expressed as

$$\tilde{E}_1(z,t) = A_1(z,t)\exp[i(k_1 z - \omega_1 t)] + c.c. \tag{2a}$$

$$\tilde{E}_2(z,t) = A_2(z,t)\exp[i(-k_2 z - \omega_2 t)] + c.c. \tag{2b}$$

$$\tilde{E}_3(z,t) = A_3(z,t)\exp[i(-k_3 z - \omega_3 t)] + c.c. \tag{2c}$$

$$\tilde{E}_4(z,t) = A_4(z,t)\exp[i(k_4 z - \omega_4 t)] + c.c. \tag{2d}$$

Similarly, the acoustic field can be described in terms of the material density distribution as

$$\tilde{\rho}(z,t) = \rho_0 + \left\{\rho(z,t)\exp\left[i(qz - \Omega t)\right] + c.c.\right\} \tag{3}$$

where $\Omega=\omega_1-\omega_2$, $q=k_1+k_2$, and ρ_0 denotes the mean density of the medium.

Taking the electrostriction effect into account, the equation for the material density can be expressed by

$$\frac{\partial^2 \tilde{\rho}}{\partial t^2} - \Gamma' \nabla^2 \frac{\partial \tilde{\rho}}{\partial t} - \upsilon^2 \nabla^2 \tilde{\rho} = \nabla \cdot \mathbf{f} \tag{4}$$

where υ is the velocity of the acoustic wave and $\Gamma' = (4\eta_s/3 + \eta_b)/\rho$ is a damping parameter (Boyd, 2008), with η_s and η_b being the shear and the bulk viscosity coefficients, respectively.

The source term on the right-hand side of Eq. (4) consists of the divergence of the force per unit volume **f**, which is given by

$$\mathbf{f} = -\frac{1}{2}\varepsilon_0 \gamma_e \nabla \left\langle \tilde{E}^2 \right\rangle \tag{5}$$

with the term in the bracket denoting the electrostriction term.

Introducing Eqs. (3) and (5) into the acoustic wave equation (4) and making the slowly varying amplitude approximation, one can obtain the result

$$-2i\Omega \frac{\partial \rho}{\partial t} - i\Omega \Gamma_B \rho - 2iq\upsilon^2 \frac{\partial \rho}{\partial z} = \varepsilon_0 \gamma_e q^2 (A_1 A_2^* + A_3^* A_4 e^{i\Delta kz}) \tag{6}$$

where $\Gamma_B = q^2\Gamma'$ is the Brillouin linewidth whose reciprocal $\tau_P = 1/\Gamma_B$ gives the phonon lifetime, and $\Delta k = (k_4 + k_3) - (k_1 + k_2)$ is the phase mismatch of the four optical waves. As we have mentioned above, the two pumps are polarized in x direction, while the probe and the reflected waves are polarized in y direction, therefore there are only two terms left in the drive term of the acoustic field.

The spatial evolution of the optical waves is described by the wave equation

$$\frac{\partial^2 \tilde{E}_j}{\partial z^2} - \left(\frac{n}{c}\right)^2 \frac{\partial^2 \tilde{E}_j}{\partial t^2} = \frac{1}{\varepsilon_0 c^2} \frac{\partial^2 \tilde{P}_j}{\partial t^2} \tag{7}$$

where j=1, 2, 3 and 4, and the total nonlinear polarization which gives rise to the source term is given by

$$\tilde{P} = \varepsilon_0 \Delta\chi \tilde{E} = \varepsilon_0 \Delta\varepsilon \tilde{E} = \varepsilon_0 \rho_0^{-1} \gamma_e \tilde{\rho} \tilde{E} \tag{8}$$

Introducing Eq. (1) into the wave equation (7) and making the slowly-varying amplitude approximation, one can obtain the coupled equations for the optical waves. Combining the acoustic wave equation (6), the coupled-wave equations for the optical fields and the acoustic wave can be obtained as

$$\left(\frac{\partial}{\partial z} + \frac{n_x}{c}\frac{\partial}{\partial t}\right) A_1 = i g_o \rho A_2 \tag{9a}$$

$$\left(-\frac{\partial}{\partial z} + \frac{n_x}{c}\frac{\partial}{\partial t}\right) A_2 = i g_o \rho^* A_1 \tag{9b}$$

$$\left(-\frac{\partial}{\partial z}+\frac{n_y}{c}\frac{\partial}{\partial t}\right)A_3 = ig_o\rho^* A_4 e^{i\Delta kz} \tag{9c}$$

$$\left(\frac{\partial}{\partial z}+\frac{n_y}{c}\frac{\partial}{\partial t}\right)A_4 = ig_o A_3\rho e^{-i\Delta kz} \tag{9d}$$

$$\left(\frac{\partial}{\partial t}+\frac{\Gamma_B}{2}\right)\rho = ig_a\left(A_1 A_2^* + A_3^* A_4 e^{i\Delta kz}\right) \tag{9e}$$

The above Eqs. (9) are just the coupled-wave equations for the optical fields and the acoustic wave in the Brillouin enhanced four-wave mixing process, where n_x and n_y are refractive indexes for the two axes of the polarization-maintaining fiber; g_o and g_a are coupling coefficients of optical wave and acoustic wave, respectively, and $g_B=4g_o g_a/\Gamma_B$ is the Brillouin gain factor. Note that when deducing Eq. (9e) the term describing the propagation of the acoustic wave in Eq. (6) has been omitted because the velocity of the acoustic wave is far smaller than that of light.

2.2 Phase matching condition

Next we will discuss the phase matching condition for this interaction process. Fig. 2 shows the wave vector mismatch of the four optical waves, according to which one can obtain the relationship between the four optical wave vectors

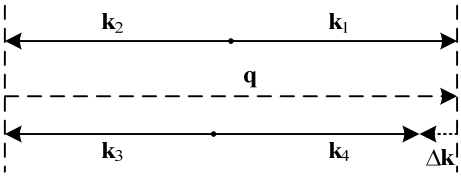

Fig. 2. Wave vector mismatch of the four optical waves.

$$\Delta\mathbf{k} = (\mathbf{k}_4 - \mathbf{k}_3) - (\mathbf{k}_1 - \mathbf{k}_2) \tag{10}$$

Therefore the magnitude of the phase mismatch is given by

$$\begin{aligned}\Delta k &= (k_4 + k_3) - (k_1 + k_2)\\ &= \left(\frac{\omega_4}{\upsilon_y}+\frac{\omega_3}{\upsilon_y}\right)-\left(\frac{\omega_1}{\upsilon_x}+\frac{\omega_2}{\upsilon_x}\right)\\ &\approx \frac{2n_y\omega_3}{c}-\frac{2n_x\omega_2}{c}\\ &= \frac{2n_y}{c}\cdot\Delta\omega\end{aligned} \tag{11}$$

where

$$\Delta\omega = \omega_3 - \frac{n_x}{n_y}\omega_2 \tag{12}$$

and we have made the assumption that $\omega_4 \approx \omega_3$ and $\omega_1 \approx \omega_2$, respectively.

If the frequency of the probe wave ω_3 is chosen to ensure that the condition of perfect phase matching, i.e., $\Delta k=0$ is satisfied, then ω_3 will take the value

$$\omega_3 = \frac{n_x}{n_y}\omega_2 \tag{13}$$

and the birefringence-induced frequency shift can be obtained as

$$\Delta\omega_{Bire} = \omega_3 - \omega_2 = \frac{\Delta n}{n}\omega_2 \tag{14}$$

or

$$\Delta\nu_{Bire} = \frac{\Delta n}{n}\nu \tag{15}$$

where $\Delta n=n_x-n_y$ is the birefringence of the polarization-maintaining fiber.

2.3 Analytic solution for steady uniform Brillouin grating

In the case of steady Brillouin grating generated by two continuous-wave (CW) pumps, all the time derivatives in the coupled-wave equations (9) are considered to be zero. We treat the simple case of uniform Brillouin grating without pump depletion, which indicates that the intensities of the two pump waves are unaffected during the interaction; while the probe wave and the reflected waves are both weak so that the acoustic wave generated by the two pumps does not affected by the probe wave. Therefore the driving term of the acoustic wave caused by the probe and the reflected waves in Eq. (9e) can be dropped and the amplitudes A_1 and A_2 of the pump waves can be considered as a constant in the coupled-wave equations, which then reduce to the simpler set for the probe and reflected waves and the acoustic wave:

$$\frac{\mathrm{d}A_3}{\mathrm{d}z} = -ig_o A_4 \rho^* e^{i\Delta kz} \tag{16a}$$

$$\frac{\mathrm{d}A_4}{\mathrm{d}z} = ig_o A_3 \rho e^{-i\Delta kz} \tag{16b}$$

$$\frac{\Gamma_B}{2}\cdot\rho = ig_a A_1 A_2^* \tag{16c}$$

By introducing Eq. (16c) into Eqs. (16a) and (16b), we obtain

$$\frac{\mathrm{d}A_3}{\mathrm{d}z} = K_1 A_4 e^{i\Delta kz} \tag{17a}$$

$$\frac{dA_4}{dz} = K_2 A_3 e^{-i\Delta kz} \tag{17b}$$

where

$$K_1 = -\frac{1}{2} g_B A_1^* A_2 \tag{18a}$$

$$K_2 = -\frac{1}{2} g_B A_1 A_2^* \tag{18b}$$

where $g_B=4g_o g_a/\Gamma_B$ is the Brillouin gain factor.

The general solution for Eqs. (17) can be written as follows:

$$A_3(z) = (C_1 e^{gz} + C_2 e^{-gz}) e^{i\Delta kz/2} \tag{19a}$$

$$A_4(z) = (D_1 e^{gz} + D_2 e^{-gz}) e^{-i\Delta kz/2} \tag{19b}$$

Where g, which is determined by $g^2=K_1K_2-(\Delta k)^2/4$, gives the rate of spatial variation of the fields and C_1, C_2, D_1, and D_2 are constants whose values depend on the boundary conditions.

Substituting the solutions (19a) and (19b) into Eqs. (17), since the resulting equations must hold for all values of z, the terms that vary as z and must each maintain the equality separately; the coefficients of these terms thus must be related by the following independent equations:

$$C_1(g + \frac{1}{2} i\Delta k) = K_1 D_1 \tag{20a}$$

$$C_2(g - \frac{1}{2} i\Delta k) = -K_1 D_2 \tag{20b}$$

Two additional relations among the quantities C_1, C_2, D_1, and D_2 come from the appropriate boundary conditions:

$$A_3(L) = (C_1 e^{gL} + C_2 e^{-gL}) e^{i\Delta kL/2} \tag{21a}$$

$$A_4(0) = D_1 + D_2 = 0 \tag{21b}$$

The values of C_1, C_2, D_1, and D_2 can be easily evaluated by solving the four independent linear Eqs. (21), and the solutions for Eqs. (17a) and (17b) thus can be obtained as

$$A_3(z) = A_3(L) \cdot \frac{2g\cosh(gz) - i\Delta k \sinh(gz)}{2g\cosh(gL) - i\Delta k \sinh(gL)} \cdot e^{-i\Delta k(L-z)/2} \tag{22a}$$

$$A_4(z) = A_3(L) \cdot \frac{2K_2 \sinh(gz)}{2g\cosh(gL) - i\Delta k \sinh(gL)} \cdot e^{-i\Delta k(L+z)/2} \tag{22b}$$

Therefore for a steady Brillouin grating, the analytic solution for the reflectivity R which is defined by

$$R = \frac{I_4(L)}{I_3(L)} \tag{23}$$

can be finally obtained as

$$R = \frac{\sinh^2(gL)}{\cosh^2(gL) - \Delta k^2 / (4K_1K_2)} \tag{24}$$

The Eq. (24) is just the analytic expression for Brillouin grating spectrum under weak probe condition, from which the reflectivity of a Brillouin grating in a polarization-maintaining fiber can be easily obtained. It should be noted that the Brillouin grating spectrum under weak probe condition, which is described by Eq. (24), is exactly the same as that of a fiber Bragg grating (Erdogan, 1997).

3. Simulations of steady Brillouin grating spectra with a strong probe wave

As we have mentioned above, the Brillouin grating spectrum is the same as the fiber Bragg grating under the condition of a weak probe wave and can be easily obtained through Eq. (24); however, it is not the case for a strong probe wave that can considerably modify the Brillouin grating, therefore numerical simulations by solving the coupled-wave equations (9) must be carried out in order to obtain the Brillouin grating spectrum. In this section, we will focus on numerical studies of the steady Brillouin grating spectrum which is generated by two counter-propagating CW pumps for the strong probe regime that can't be reached by the analytic solution. For all of these simulations some parameters like the Brillouin linewidth, the fiber length and powers of the two pump waves take their values listed in Table 1 otherwise they are stated in particular.

Parameter	$\Gamma_B/2\pi$	L	P_1	P_2	g_B
Value	30MHz	1m	0.1W	0.1W	2.5×10^{-11} m/W

Table 1. Some common parameters used for simulations.

3.1 Time traces of reflectivity

Fig. 3 shows the time trace of reflectivity under phase matching condition for coherent anti-Stokes Brillouin scattering case, where the four figures (a), (b), (c) and (d) correspond to a probe power of 1, 10, 30 and 50W, respectively. It can be seen from these figures that at a lower probe power, the reflection intensity increases monotonously with time and then tends to a fixed value; however, it oscillates several times before turning into a constant value as the probe power increases, and it will oscillate more times at a higher probe power. The oscillation of the reflection in time domain at high probe power can be attributed to the relaxation of the acoustic field.

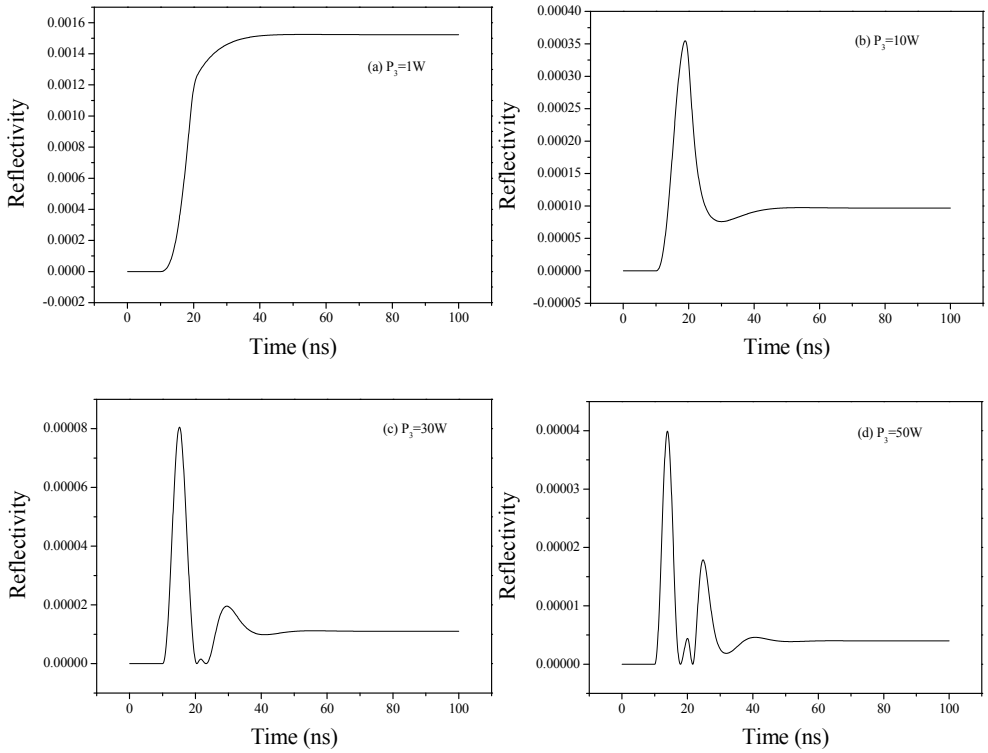

Fig. 3. Time traces of reflectivity under phase matching condition for coherent anti-Stokes Brillouin scattering case.

The time trace of reflectivity under phase matching condition for coherent Stokes Brillouin scattering case is shown in Fig. 4, where the four figures (a), (b), (c) and (d) correspond to a probe power of 1, 10, 20 and 28W, respectively. For the coherent Stokes Brillouin scattering case, the time evolution behaves similarly as that for the coherent anti-Stokes Brillouin scattering case, however, it will take a much longer time for the reflection to reach steady than that for the coherent anti-Stokes Brillouin scattering case, especially with a high probe power. And the higher the probe power is, the longer time it will oscillate before reaching a steady value.

3.2 Brillouin grating spectra

First we do simulations in weak probe regime for both coherent Stokes and anti-Stokes Brillouin scattering cases and compare the results with the analytic solution in Fig. 5. In this simulation a probe power of 0.01W was used. It is seen that for both coherent Stokes and anti-Stokes Brillouin scattering cases, the simulation results agree very well with the analytic solution.

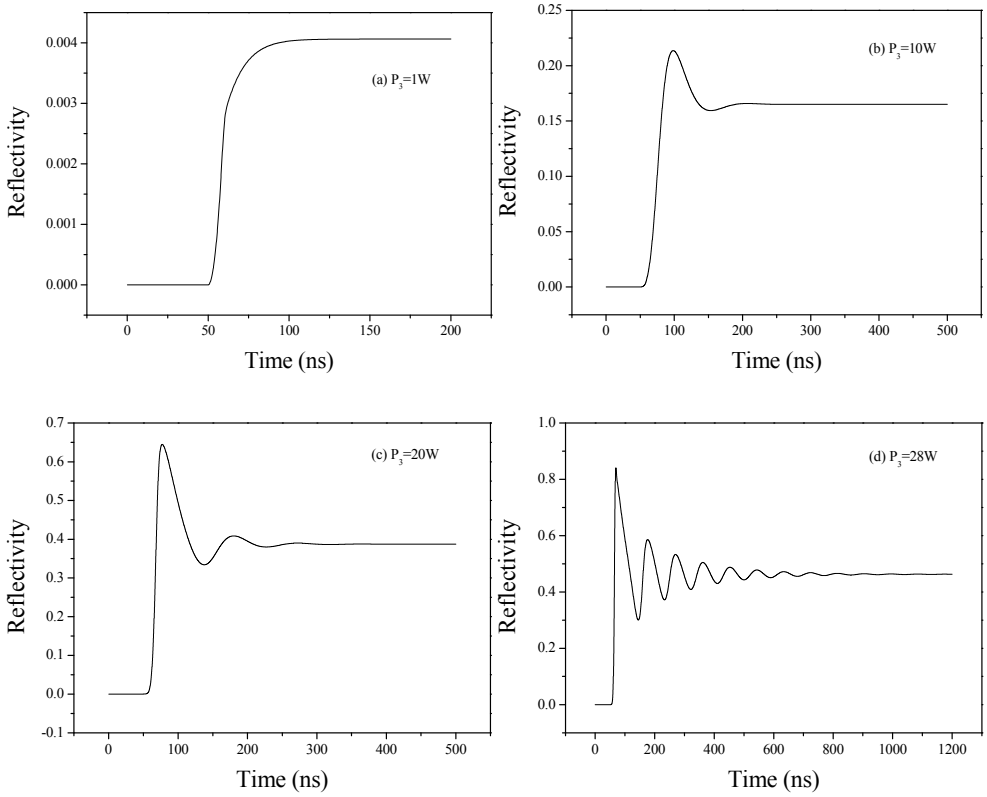

Fig. 4. Time traces of reflectivity under phase matching condition for coherent Stokes Brillouin scattering case.

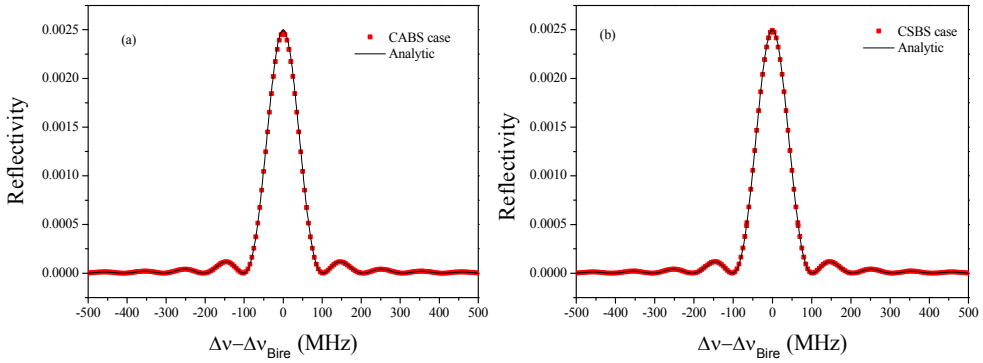

Fig. 5. Comparison between simulation and analytic results for (a) coherent anti-Stokes Brillouin scattering (CABS) and (b) coherent Stokes Brillouin scattering (CSBS).

Fig. 6 shows the normalized reflected spectrum at different probe powers for coherent anti-Stokes Brillouin scattering case. In this figure different curves correspond to a probe power of 0.1, 5, 10 and 20W, respectively. It can be seen from the figure that for all of these cases, the spectra are symmetrical and maximized at line center. The side-lobes vanish gradually as the probe power increases, while the spectrum broadens evidently and tends to a standard Lorentzian shape.

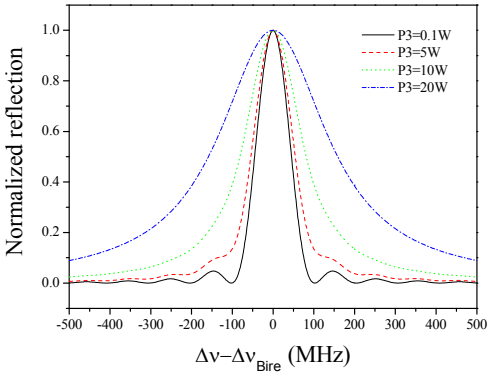

Fig. 6. Reflected spectrum at different probe powers for coherent anti-Stokes Brillouin scattering case.

As for the coherent Stokes Brillouin scattering case, we obtain some results that are very different. The normalized reflected spectrum at different probe powers for coherent Stokes Brillouin scattering case are shown in Fig. 7, where different curves correspond to a probe power of 0.1, 5, 10 and 20W, respectively. From Fig. 7 it can be seen that the spectra are also symmetrical and behave similarly as that for coherent anti-Stokes Brillouin scattering case at a low probe power. However, as the probe power becomes higher, the side-lobes grow remarkably and even exceed the line center, so that the maximum reflectivity shifts from line center to the first side-lobe.

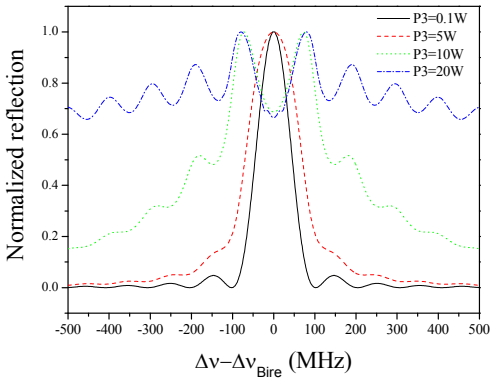

Fig. 7. Reflected spectrum at different probe powers for coherent Stokes Brillouin scattering case.

Fig. 8 shows the reflectivity as a function of probe power under phase matching condition. It is clearly seen that for the coherent anti-Stokes Brillouin scattering case, in which the acoustic wave will be depleted by the probe wave, the reflectivity decreases as the probe power becomes higher, and the maximum reflectivity is not larger than 0.25%. While for the coherent Stokes Brillouin scattering case, in which the acoustic wave will be enhanced by the probe wave, the reflectivity is much higher and increases with the probe power.

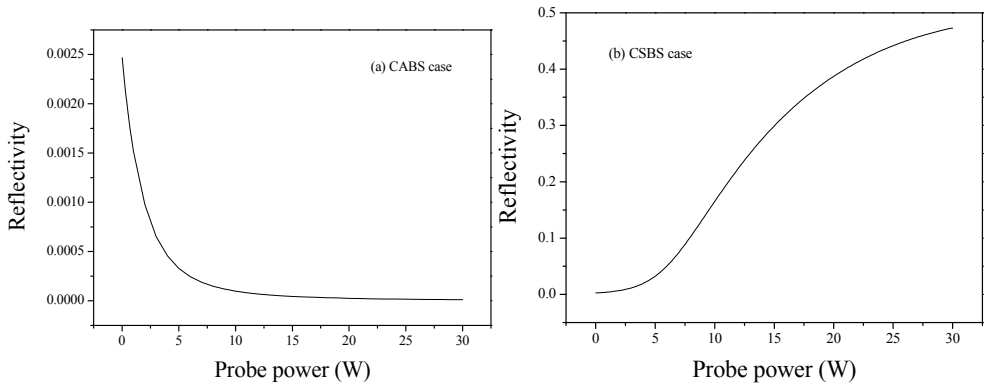

Fig. 8. Reflectivity as a function of probe power under phase matching condition for (a) coherent anti-Stokes Brillouin scattering (CABS) and (b) coherent Stokes Brillouin scattering (CSBS).

Fig. 9 shows the spectrum width as a function of probe power, where (a) is the result of coherent anti-Stokes Brillouin scattering case, while (b) is that of coherent Stokes Brillouin scattering case. It is seen that for both cases the spectrum width remains unchanged in the weak probe regime and becomes larger rapidly as the probe power increases in the strong probe regime.

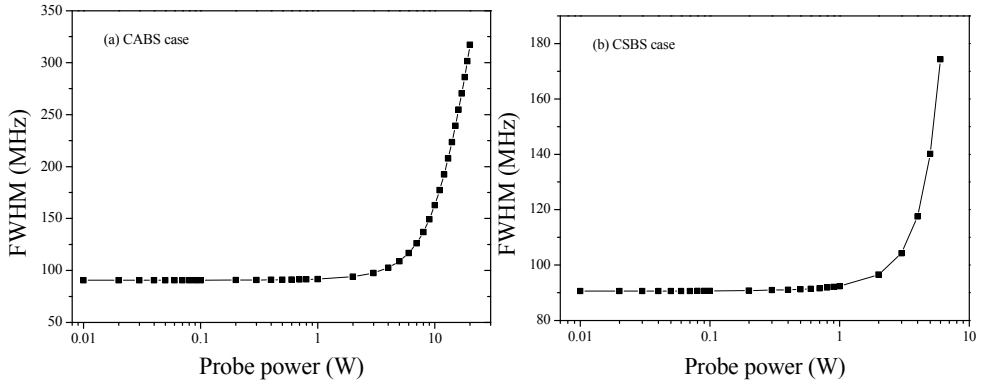

Fig. 9. Spectrum width as a function of probe power for (a) coherent anti-Stokes Brillouin scattering (CABS) and (b) coherent Stokes Brillouin scattering (CSBS).

4. Experimental study of transient Brillouin grating spectrum

In this section, we will experimentally investigate the reflected spectrum of transient Brillouin grating that is generated by two pump pulses. As shown in Fig. 10, the frequency of pump 1 is higher than that of pump 2 by a Ω_B of optical fiber, and the Brillouin grating has the same motion direction as pump 1. Two pump pulses are launched into the slow axis of a polarization-maintaining fiber, and the probe pulse immediately following pump 2 pulse (the leading edge of probe pulse overlapping with trailing edge of pump 2 pulse) is launched into the fast axis to read the Brillouin grating. Because the probe pulse counter-propagates with the Brillouin grating, coherent anti-Stokes Brillouin scattering could occur when the probe pulse interacts with the Brillouin grating, and consequently the scattered light frequency is higher than that of probe pulse by a Ω_B .

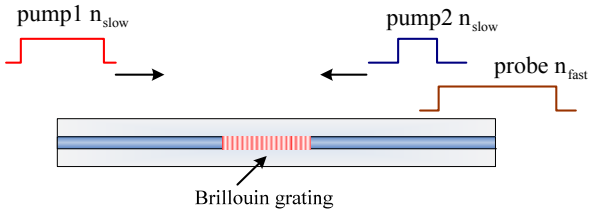

Fig. 10. Schematic diagram of transient Brillouin grating generation and reading using two pump pulses and a probe pulse.

The experimental setup is shown in Fig. 11. Two narrow linewidth (3 kHz) fiber lasers operating at 1550 nm are used to provide the pump1 and pump2, respectively, and their frequency difference is locked by a microwave frequency counter. A tunable laser with a wavelength resolution of 0.1 pm is used as probe wave. The frequency difference between pump1 and probe is monitored and recorded by a 45-GHz bandwidth high-speed detector and a 44-GHz electrical spectrum analyzer. Three high extinction-ratio (ER) electro-optic modulators (> 45 dB) are used to generate pump 1, pump 2 and probe pulses. The power of

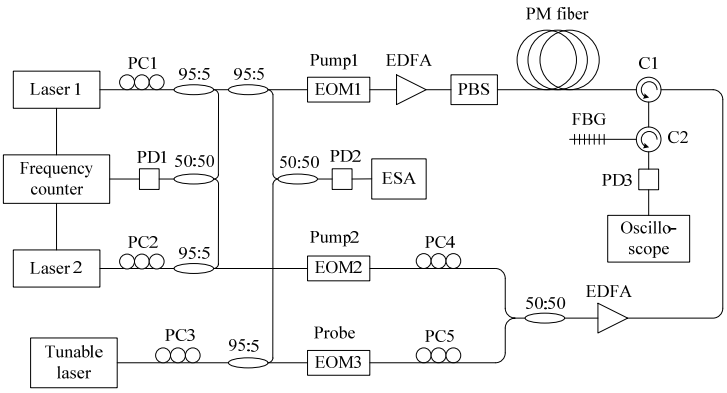

Fig. 11. Experimental setup. PC: polarization controller, EOM: electro-optic modulator, PBS: polarization beam splitter, C: circulator, PD: photo-detector, EDFA: Erbium-doped fiber amplifier, ESA: electrical spectrum analyzer, FBG: fiber Bragg grating.

pump 1 pulse, pump 2 pulse and probe pulse in the PMF are about 0.4W, 30 W and 30 W, respectively. A tunable fiber Bragg grating with a bandwidth of 0.2 nm is used to filter out the transmitted pump1 pulse. A Panda PMF is used in experiment, whose nominal beat-length is smaller than 5 mm at 1550 nm with a Brillouin frequency shift of 10.871 GHz at room temperature.

Then we investigated the Brillouin grating spectra with different grating lengths. The effective length of the transient Brillouin grating is $L_B = (t_{P1} + t_{P2})c/4n$, where t_{P1} and t_{P2} are the pulse widths of pump 1 and pump 2, respectively. In experiment, t_{P2} was fixed at 2 ns and t_{P1} was increased from 2 ns to 6 ns to increase the effective length of the transient Brillouin grating from 0.2 m to 0.4 m. The probe pulse width of 6 ns and 8 ns were chosen to read the Brillouin grating, and the measured reflected spectra of the transient Brillouin grating are shown in Fig. 12. For the case of a 2-ns pump 1 pulse and a 2-ns pump 2 pulse, the effective length of the transient Brillouin grating is 0.2 m and the measured spectra are shown in Fig. 12 (a), which fit well with a Gaussian profile. The intensity of the acoustic wave is determined by the interaction time of the pump and the Stokes waves, and thus the

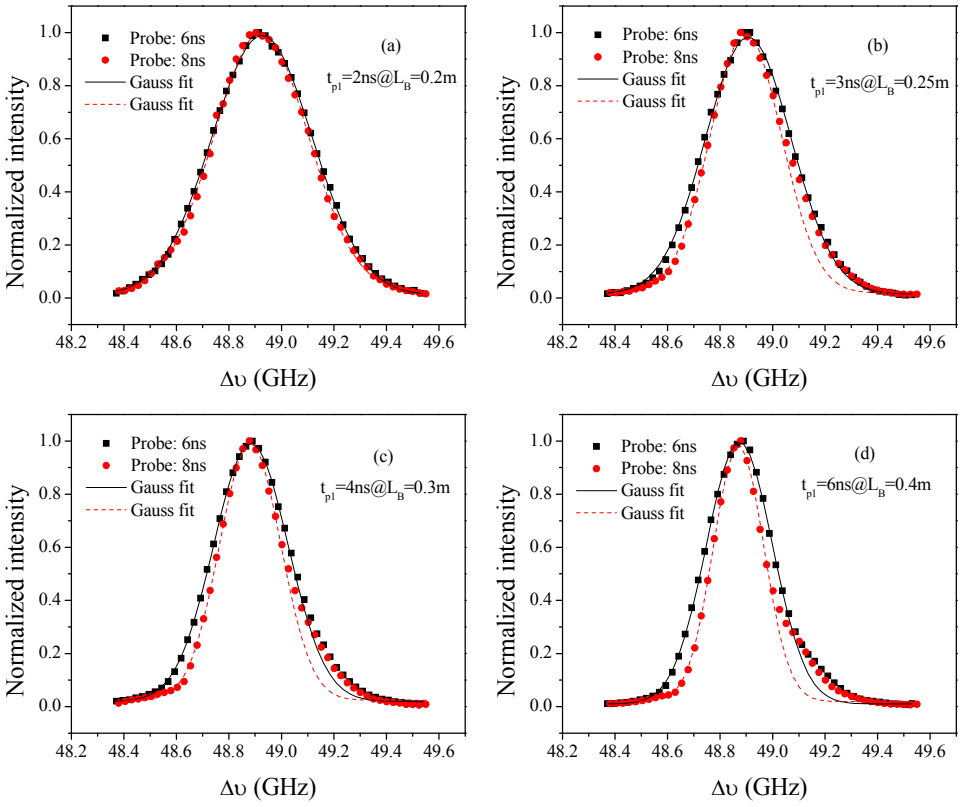

Fig. 12. Measured Brillouin grating spectra with 6 ns and 8 ns probe pulse with different pump 1 pulse-widths of (a) 2 ns, (b) 3 ns, (c) 4 ns, (d) 6 ns. Pump 2 pulse width is constant at 2 ns. (Dong et al., 2010b, with permission from OSA)

generated transient Brillouin grating is a nonuniform-grating with Δn maximizing at the center and decreasing toward two sides. This nonuniform apodization of transient Brillouin grating results in a Gaussian spectrum without side lobes, which are expected in a uniform-grating.

The measured spectrum is the convolution of the probe pulse spectrum and the intrinsic Brillouin grating spectrum. The intrinsic Brillouin grating spectrum can be obtained from deconvoluting the probe pulse spectrum out of the measured spectra, and the spectral widths (FWHM) are plotted in Fig. 13. The black curve shows the FWHM spectrum width of weak fiber Bragg grating described in (Erdogan, 1997). For a 8-ns probe pulse, the measured spectral widths agree very well with the theory of weak fiber Bragg grating; for a 6-ns probe pulse, the experimental results also agree with the theoretical curve when the grating length is shorter than 0.3 m, while the discrepancy from the theory at 0.4 m originates from the effective reading-length of the 6-ns probe pulses. These results directly prove that the moving Brillouin grating and the static fiber Bragg grating follow the same basic theory.

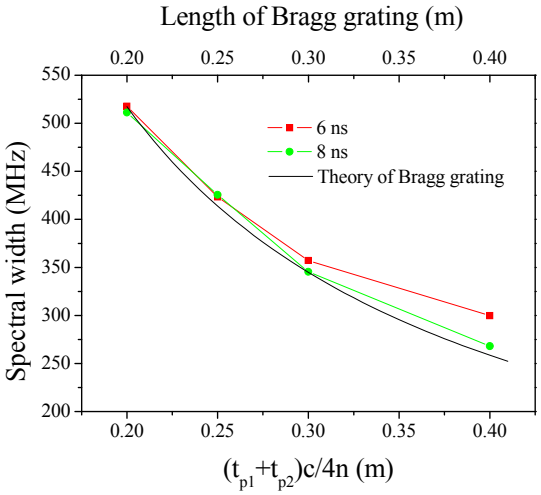

Fig. 13. The intrinsic Brillouin grating spectral width as a function of length. (Dong et al., 2010b, with permission from OSA)

The other important characteristic of the transient Brillouin grating is the acoustic wave relaxation or grating decay. The Brillouin grating is created through electrostriction effect and can only be sustained by keeping the two pump waves. After removing the pump waves, the Brillouin grating will exponentially decay, which characterizes an intrinsic Lorentzian Brillouin gain spectrum. In our scheme as shown in Fig. 10, pump 2 pulse is fixed at 2 ns and pump 1 pulse width is increased to prolong the grating length. The Brillouin grating is generated following pump 2 pulse from the right end to the left end, and the intensity of the whole Brillouin grating exhibit a slope due to the acoustic wave decay. For the probe pulse immediately following pump 2 pulse, the front of the probe pulse always read the strongest part of the grating, while the rear of the probe pulse always read the decayed part, which causes the asymmetry of the spectra especially for long gratings as shown in Fig. 12. It is clearly seen that for long gratings the low-frequency side still agrees

well with Gaussian profile, while the high-frequency side has a discrepancy and shows a Lorentzian-like wing, which comes from the apodization of the Brillouin grating induced by acoustic wave decay.

To further demonstrate the effect of the apodization of the Brillouin grating induced by the acoustic wave decay, we switched the pulse width of pump 1 and pump 2 pulses with probe pulse still immediately following pump 2 pulse. Figure 14 shows the measured Brillouin grating spectrum with a 2-ns pump 1 pulse, a 10-ns pump 2 pulse and a 6-ns probe pulse. In this case, the Brillouin grating is created following pump 1 pulse from the left end to the right end, and both of the front and the rear of the probe pulse read the decayed grating. We see that the measured spectrum agrees with a Lorentzian profile, which indicates that the acoustic wave decay play an important role in this case. For the case of a 2-ns pump 1 and a 2-ns pump 2, the interaction duration is much smaller than the phonon lifetime, and consequently the grating decay can be neglected, so that the spectra have a Gaussian profile as shown in Fig. 12 (a).

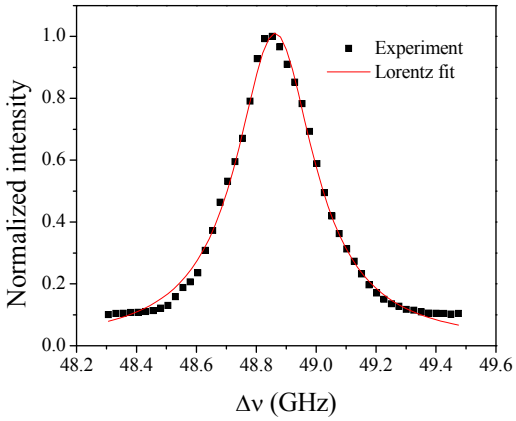

Fig. 14. Measured Brillouin grating spectrum with a 2-ns pump 1 pulse, a 10-ns pump 2 pulse and a 6-ns probe pulse. (Dong et al., 2010b, with permission from OSA)

5. Applications of Brillouin gratings

5.1 Distributed birefringence measurement of polarization-maintaining fibers

Polarization-maintaining fibers have attracted considerable interest in telecommunication and optical sensing community. The phase modal birefringence of a polarization-maintaining fiber is an important parameter for its applications. During the fabrication of the polarization-maintaining fibers, due to the non-uniformity of the materials and environmental condition change in fiber drawing process, it is inevitable to introduce birefringence variation along the fiber. Many methods have been proposed to measure the birefringence of polarization-maintaining fibers (Flavin et al., 2002; Hlubina et al., 2007; Kim et al., 2003; Olsson et al., 1998). However, these methods can only give the average birefringence of the test fibers, and can not characterize the birefringence variation along the fiber. In this section, we study a truly distributed birefringence measurement of polarization-maintaining fibers based on a transient Brillouin grating.

According to the phase matching condition $\Delta\nu_{Bire} = \Delta n\nu / n_g$, the birefringence of the polarization-maintaining fibers can be calculated from the birefringence-induced frequency shift $\Delta\nu_{Bire}$, which can be obtained through the reflected spectrum of the Brillouin grating. In our birefringence measurement scheme, two short counter-propagating pump1 and pump2 pulses, where the frequency of pump1 is larger than that of pump2 by a Brillouin frequency shift ω_B, are launched into one axis of a polarization-maintaining fiber to excite a Brillouin grating through stimulated Brillouin scattering process. Following pump2 pulse, a long probe pulse is launched into the other axis, and energy from the probe pulse could be partly reflected at the expense of Brillouin grating. A maximum reflected probe signal could be obtained when the frequency difference between the pump2 and probe satisfies the phase matching condition.

There are two schemes to perform the birefringence measurement: one is that the Brillouin grating is excited in the fast axis and probed in the slow axis; and the second is that the Brillouin grating is excited in the slow axis and probed in the fast axis, shown as Fig. 15 (a) and (b), respectively. For both cases, the birefringence-induced frequency shift between the pump2 and probe are the same, which is proportional to the local birefringence. As can be seen in the following context, the birefringence induced frequency shifts are about 43 GHz and 49 GHz for Bow-tie and Panda fibers, respectively, which are difficulty to be measured directly. In order to precisely measure the birefringence frequency shift and thus accurately calculate the birefringence, we choose the second scheme. In this scheme, the frequency difference between the pump1 and probe is smaller than the birefringence-induced frequency shift by a Brillouin frequency shift, and can be measured by a high-speed photo-detector and an electrical spectrum analyzer, as shown in Fig. 11. So the actual birefringence-induced frequency shift equals the measured frequency difference between pump1 and probe plus a Brillouin frequency shift.

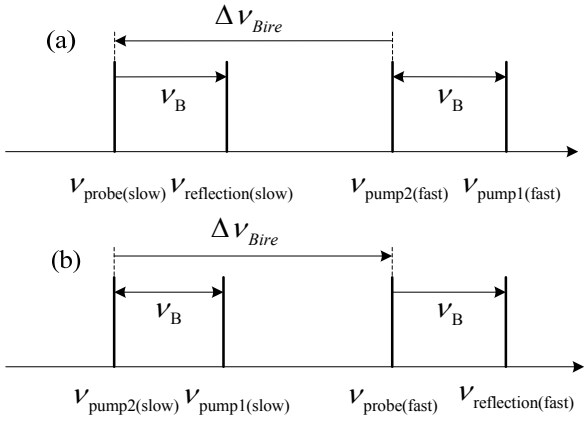

Fig. 15. Frequency relationship of pump1, pump2, probe and reflection: (a) the Brillouin grating is excited in the fast axis and probed in the slow axis, and (b) the Brillouin grating is excited in the slow axis and probed in the fast axis.

An 8-m Bow-tie fiber (HB1500T) and an 8-m Panda fiber (PM-1550-HP) are used as fibers under test. The Bow-tie fiber has a mode field diameter of 10.5 μm and its nominal beat-

length is smaller than 2 mm at 633 nm, whose Brillouin frequency shift is 10.815 GHz at room temperature and Brillouin spectrum width is 61 MHz. The Panda fiber has a mode field diameter of 10.5 μm and its nominal beat-length is smaller than 5 mm at 1550 nm, with a Brillouin frequency shift of 10.871 GHz at room temperature and a Brillouin spectrum width of 60 MHz. Both fibers were in loose state to avoid strain-induced birefringence. In experiment, pump 1 and pump 2 pulses are both set at 2 ns, which give a 20-cm spatial resolution. The measured Brillouin grating spectrum is the convolution of the probe pulse spectrum and the intrinsic Brillouin grating spectrum, and thus a longer probe pulse can give narrower spectrum and better frequency and birefringence accuracy. However, the probe pulse width is limited by the phonon lifetime, which is ~10 ns in the optical fiber, so an 8-ns probe pulse is used to obtain the Brillouin grating spectrum.

Figure 16 show the measured results of Bow-tie and Panda fibers, where the delay step between the two pump pulses is set at 1 ns corresponding to 10 cm/point. For the Bow-tie fiber, the birefringence has a characteristic periodic variation with a period of ~3.5m, and exhibits an increasing tendency along the fiber, which indicates that there could be another long period. Different periods could correspond to different disturbance factors during the fiber drawing process; over the 8-m length the birefringence variation range is ~2.4×10^{-6}. For the Panda fiber, there is no obvious periodic characteristic within the measured length except a dip at the location of ~3 m; over the 8-m length the birefringence variation range is ~1.3×10^{-6}. The measured central frequency uncertainty of the Brillouin spectrum is ~3 MHz, which corresponds to a measured birefringence accuracy of ~2×10^{-8}.

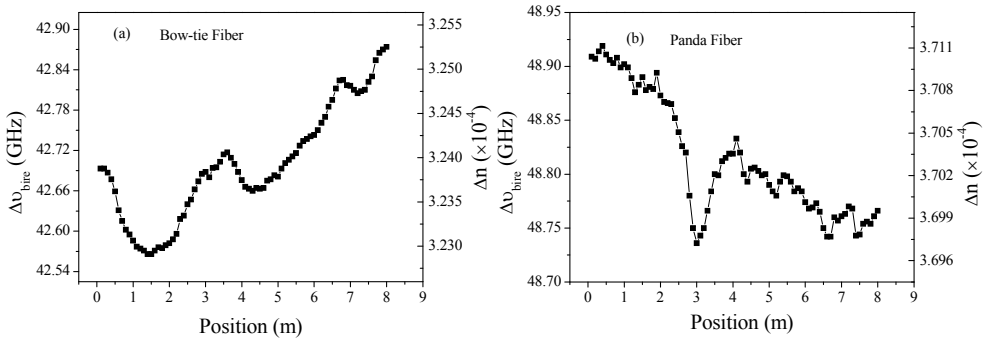

Fig. 16. Measured distributed birefringence of (a) a 8-m Bow-tie fiber and (b) a 8-m Panda fiber. (Dong et al., 2010a, with permission from OSA)

5.2 Distributed simultaneous temperature and strain measurement

Brillouin scattering based distributed fiber sensors have shown the capability of distributed strain and temperature measurement. However, since both strain and temperature can produce a Brillouin frequency shift change, the Brillouin based sensor suffers from the cross sensitivity. Normally it can not be determined that a Brillouin frequency shift change is induced by a change in temperature or strain. In this section, we study simultaneous strain and temperature measurement using Brillouin scattering and birefringence in a polarization-maintaining fiber.

Brillouin scattering is an inelastic light scattering with acoustic phonons and undergoes a frequency shift after collision. Brillouin frequency shift is given by

$$\nu_B = 2nV_a/\lambda \tag{25}$$

where n is the refractive index, V_a is the velocity of acoustic wave, and λ is the light wavelength in vacuum. It was found that the Brillouin frequency shift increases with strain and temperature.

In a polarization-maintaining fiber, temperature and strain both can alter its birefringence, and it was found that the birefringence-induced frequency shift increases with the strain and decreases with temperature, which provides another uncorrelated mechanism to measure the temperature and strain change.

The dependences of the changes of Brillouin frequency shift and birefringence-induced frequency shift, $\Delta\nu_B$ and $\Delta\nu_{Bire}$, on strain and temperature can be expressed by

$$\begin{aligned} \Delta\nu_B &= C_B^{\varepsilon}\Delta\varepsilon + C_B^{T}\Delta T \\ \Delta\nu_{Bire} &= C_{Bire}^{\varepsilon}\Delta\varepsilon + C_{Bire}^{T}\Delta T \end{aligned} \tag{26}$$

where $\Delta\varepsilon$ and ΔT are changes in strain and temperature, respectively; C_B^{ε} and C_B^{T} are coefficients to strain and temperature related to Brillouin frequency shift, respectively; C_{Bire}^{ε} and C_{Bire}^{T} are coefficients to strain and temperature related to birefringence-induced frequency shift, respectively. The strain and the temperature can then be uniquely determined by the measured Brillouin frequency shift and birefringence-induced frequency shift, and can be given by

$$\begin{bmatrix} \Delta\varepsilon \\ \Delta T \end{bmatrix} = \frac{1}{C_B^{\varepsilon}C_{Bire}^{T} - C_B^{T}C_{Bire}^{\varepsilon}} \begin{bmatrix} C_{Bire}^{T} & -C_B^{T} \\ -C_{Bire}^{\varepsilon} & C_B^{\varepsilon} \end{bmatrix} \begin{bmatrix} \Delta\nu_B \\ \Delta\nu_{Bire} \end{bmatrix} \tag{27}$$

Here C_B^{ε}, C_B^{T} and C_{Bire}^{ε} have positive sign, while C_{Bire}^{T} has a negative sign, so $C_B^{\varepsilon}C_{Bire}^{T} - C_B^{T}C_{Bire}^{\varepsilon}$ is of a large value, which ensures a high discrimination accuracy.

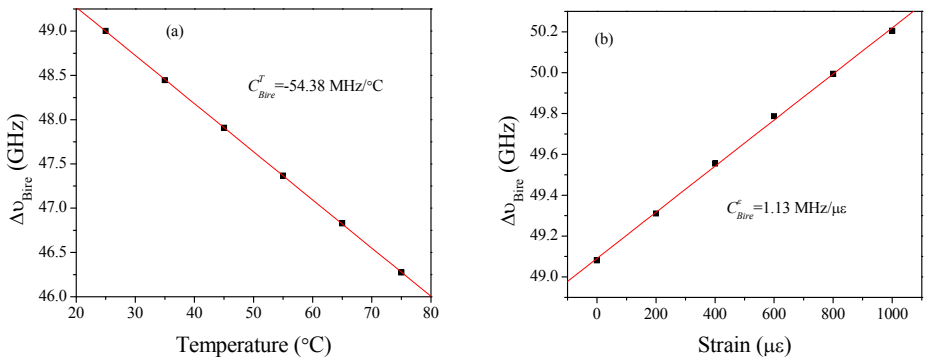

Fig. 17. The dependence of birefringence-induced frequency shift on (a) temperature and (b) strain. (Dong et al., 2010c, with permission from IEEE)

First, we measured the dependences of Brillouin frequency shift on temperature and strain, and the temperature and strain coefficients are $C_B^T = 1.12\,\text{MHz/°C}$ and $C_B^\varepsilon = 0.0482\,\text{MHz/με}$, respectively. Then we measured the dependences of birefringence-induced frequency shift on temperature and strain, and the results are shown in Fig. 17, where the fitting temperature and strain coefficients are $C_{Bire}^T = -54.38\,\text{MHz/°C}$ and $C_{Bire}^\varepsilon = 1.13\,\text{MHz/με}$, respectively.

Simultaneous measurement of strain and temperature is performed using a 6-m Panda fiber with 1-m stressed segment, 1-m heated segment and 1-m segment at room temperature and loose state in between, which is shown in Fig. 18. The applied strain is about 670 με and the heated temperature is higher than room temperature by 30 °C.

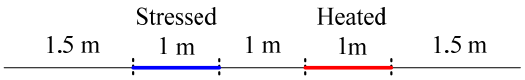

Fig. 18. Layout of the sensing fiber.

A 30/28 ns pulse pair is used to perform Brillouin frequency shift measurement and the spatial resolution is 20 cm, which is determined by the 2-ns pulse-width difference. The measured Brillouin frequency shift difference (subtracting the values at room temperature and loose state) is shown in Fig. 19 (a). The fitting uncertainty of the central frequency is 0.4 MHz, corresponding to a δT of 0.36 °C and a $\delta\varepsilon$ of 8.3 με. For birefringence-induced frequency shift measurement, the spatial resolution is determined by the effective length of the Brillouin grating, which is 20 cm for 2-ns pump pulses. A longer 6-ns probe pulse is used to provide narrower measured Brillouin grating spectrum, and thus give better frequency accuracy. The measured birefringence-induced frequency shift difference (subtracting the values at room temperature and loose state) is shown in Fig. 19 (b). The fitting uncertainty of the central frequency is 3 MHz, corresponding to a δT of 0.06 °C and a $\delta\varepsilon$ of 2.7 με. Note that the birefringence-induced frequency shift provides higher precision with respect to Brillouin frequency shift, so that the discrimination accuracy is limited by the uncertainty of Brillouin frequency shift.

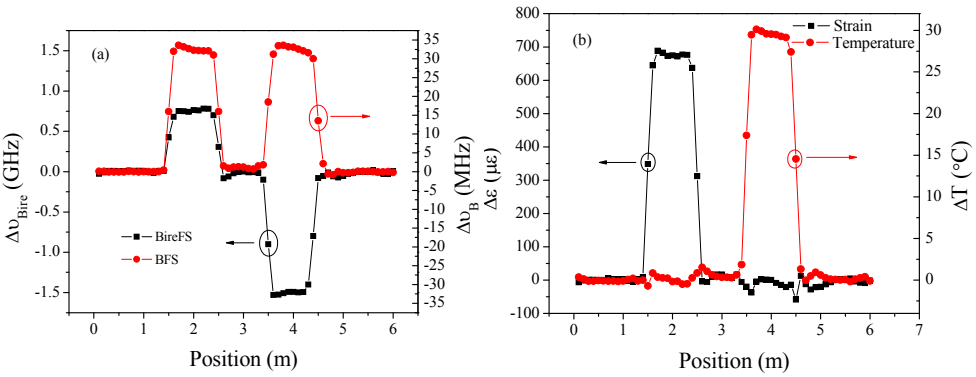

Fig. 19. (a) Measured birefringence-induced frequency shift (BireFS) and Brillouin frequency shift (BFS) and (b) calculated temperature and strain. (Dong et al., 2010c, with permission from IEEE)

6. Conclusion

First, the coupled wave equations of Brillouin enhanced four-wave mixing associated with a Brillouin grating are deduced, and the birefringence-induced frequency shift in a polarization-maintaining fiber is given through phase matching condition; in the case of weak probe, the steady uniform Brillouin grating spectrum is exactly the same as that of a fiber Bragg grating. Second, in the case of strong probe, the Brillouin grating can be considerably modified by the probe wave, resulting in that for the coherent anti-Stokes Brillouin scattering case, as the probe power increases, the reflectivity decreases and the spectrum width increases, and the spectrum profile tends to a Lorentzian shape; for the coherent Stokes Brillouin scattering case, as the probe power increases, both the reflectivity and the spectrum width increases, and the spectrum profile exhibits oscillations. Third, the transient Brillouin gratings generated by two short pump pulses have a Gaussian profile, and the acoustic wave decay can impose an apodization on the gratings. Fourth, two applications of Brillouin grating are given: for the distributed birefringence measurement of a polarization-maintaining fiber, the spatial resolution of 20 cm is obtained by using 2-ns pump pulses and the measurement accuracy can reach to 2×10^{-8}; the birefringence-induced frequency shift in a polarization-maintaining fiber shows dependences on temperature and strain, and simultaneous measurement of temperature and strain is realized by combining a conventional Brillouin fiber sensor based on Brillouin frequency shift.

7. Acknowledgment

The authors would like to thank Natural Science and Engineering Research Council of Canada (NSERC) through discovery and strategic grants and Canada Research Chair program for their financial support of this research.

8. References

Boyd, R. W. (2008). *Nonlinear Optics,* Academic Press, ISBN 978-0-12-369470-6, San Diego, USA

Cao, Y.; Lu P.; Yang Z. & Chen W. (2008). An Efficient Method of All-optical Buffering with Ultra-small Core Photonics Crystal fibers. *Opt. Express,* Vol.16, No.18, (September 2008), pp. 14142-14150, ISSN 1094-4087

Dong Y.; Bao X. & Chen L. (2009). Distributed Temperature Sensing Based on Birefringence Effect on Transient Brillouin Grating in a Polarization-maintaining Photonics Crystal Fiber. *Opt. Lett.,* Vol.34, No.17, (September 2009), pp. 2590-2592, ISSN 0146-9592

Dong Y.; Chen L. & Bao X. (2010). Truly Distributed Birefringence Measurement of Polarization-maintaining Fibers Based on Transient Brillouin Grating. *Opt. Lett.,* Vol.35, No.2, (January 2010), pp. 193-195, ISSN 0146-9592

Dong Y.; Chen L. & Bao X. (2010). Characterization of the Brillouin Grating Spectra in a Polarization-maintaining fiber. *Opt. Express,* Vol.18, No.18, (August 2010), pp. 18960-18967, ISSN 1094-4087

Dong Y.; Chen L. & Bao X. (2010). High-Spatial-Resolution Time-Domain Simultaneous Strain and Temperature Sensor Using Brillouin Scattering and Birefringence in a

Polarization-Maintaining Fiber. *IEEE Photon. Technol. Lett.,* Vol.22, No.18, (September 2010), pp. 1364-1366, ISSN 1041-1135

Flavin D. A.; McBride R. & Jones J. D. C. (2002). Dispersion of Birefringence and Differential Group Delay in Polarization-maintaining Fiber. *Opt. Lett.,* Vol.27, No.12, (June 2002), pp. 1010-1012, ISSN 0146-9592

Erdogan T. (1997). Fiber Grating Spectra. *J. Lightwave Technol.,* Vol.15, No.8, (August 1997), pp. 1277-1294, ISSN 0733-8724

Hlubina P. & Ciprian D. (2007). Spectral-domain Measurement of Phase Modal Birefringence in Polarization-maintaining Fiber. *Opt. Express,* Vol.15, No.25, (December 2007), pp. 17019-17024, ISSN 1094-4087

Kim C. S. et al. (2003). Optical Fiber Modal Birefringence Measurement Based on Lyot-Sagnac Interferometer. *IEEE Photon. Technol. Lett.,* Vol.15, No.2, (February 2010), pp. 269-272, ISSN 1041-1135

Olsson B. E.; Karlsson M. & Andrekson P. A. (1998). Polarization Mode Dispersion Measurement Using a Sagnac Interferometer and a Comparison with the Fixed Analyzer Method. *IEEE Photon. Technol. Lett.,* Vol.10, No.7, (July 1998), pp. 997-999, ISSN 1041-1135

Song K. Y.; Zou W.; He Z. & Hotate K. (2008). All-optical Dynamic Grating Generation Based on Brillouin Scattering in a Polarization-maintaining Fiber. *Opt. Lett.,* Vol.33, No.9, (May 2008), pp. 926-928, ISSN 0146-9592

Song K. Y.; Zou W.; He Z. & Hotate K. (2009). Optical Time-domain Measurement of Brillouin Dynamic Grating Spectrum in a Polarization-maintaining Fiber. *Opt. Lett.,* Vol.34, No.9, (May 2009), pp. 1381-1383, ISSN 0146-9592

Song K. Y.; Lee K. & Lee S. B. (2009). Tunable Optical Delays Based on Brillouin Dynamic Grating in Optical Fibers. *Opt. Express,* Vol.17, No.12, (June 2009), pp. 10344-10349, ISSN 1094-4087

Song K. Y. & Yoon H. J. (2010). High-resolution Brillouin Optical Time Domain Analysis Based on Brillouin Dynamic Grating. *Opt. Lett.,* Vol.35, No.17, (January 2010), pp. 52-54, ISSN 0146-9592

Zhu, Z.; Gauthier D. G. & Boyd R. W. (2007). Stored Light in an Optical Fiber via Stimulated Brillouin Scattering. *Science,* Vol.318, No.5857, (December 2007), pp. 1748-1750, ISSN 0036-8075

Zou W.; He Z. & Hotate K. (2009). Complete Discrimination of Strain and Temperature Using Brillouin Frequency Shift and Birefringence in a Polarization-maintaining Fiber. *Opt. Express,* Vol.17, No.3, (February 2009), pp. 1248-1255, ISSN 1094-4087

Zou W.; He Z.; Song K. Y. & Hotate K. (2009). Correlation-based Distributed Measurement of a Dynamic Grating Spectrum Generated in Stimulated Brillouin Scattering in a Polarization-maintaining Optical Fiber. *Opt. Lett.,* Vol.34, No.7, (April 2009), pp. 1126-1128, ISSN 0146-9592

Zou W.; He Z. & Hotate K. (2010). Demonstration of Brillouin Distributed Discrimination of Strain and Temperature Using a Polarization-maintaining Optical Fiber. *IEEE Photon. Technol. Lett.,* Vol.22, No.8, (April 2010), pp. 526-528, ISSN 1041-1135

Kalosha V.P.; Li W.; Wang F.; Chen L. & Bao X. (2008). Frequency-shifted Light Storage via Stimulated Brillouin Scattering in Optical Fibers. *Opt. Lett.,* Vol.33, No.23, (December 2008), pp. 2848-2850, ISSN 0146-9592

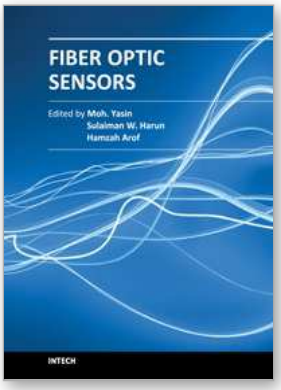

Fiber Optic Sensors

Edited by Dr Moh. Yasin

ISBN 978-953-307-922-6
Hard cover, 518 pages
Publisher InTech
Published online 22, February, 2012
Published in print edition February, 2012

This book presents a comprehensive account of recent advances and researches in fiber optic sensor technology. It consists of 21 chapters encompassing the recent progress in the subject, basic principles of various sensor types, their applications in structural health monitoring and the measurement of various physical, chemical and biological parameters. It also highlights the development of fiber optic sensors, their applications by providing various new methods for sensing and systems, and describing recent developments in fiber Bragg grating, tapered optical fiber, polymer optical fiber, long period fiber grating, reflectometry and interefometry based sensors. Edited by three scientists with a wide knowledge of the field and the community, the book brings together leading academics and practitioners in a comprehensive and incisive treatment of the subject. This is an essential reference for researchers working and teaching in optical fiber sensor technology, and for industrial users who need to be aware of current developments and new areas in optical fiber sensor devices.

InTech Europe
University Campus STeP Ri
Slavka Krautzeka 83/A
51000 Rijeka, Croatia
Phone: +385 (51) 770 447
Fax: +385 (51) 686 166
www.intechopen.com

InTech China
Unit 405, Office Block, Hotel Equatorial Shanghai
No.65, Yan An Road (West), Shanghai, 200040, China
中国上海市延安西路65号上海国际贵都大饭店办公楼405单元
Phone: +86-21-62489820
Fax: +86-21-62489821